Check for updates

Advanced Functional Materials

ADVANCED FUNCTIONAL MATERIALS
www.afm-journal.de

RESEARCH ARTICLE

Engineering Core–Shell Interfaces with Hierarchical Mass Transport for Dendrite-Free and Highly Reversible Zn Anodes

Ming Zhao[1] | Yanjing Wang[1] | Zhihao Li[1] | Le Zhou[1] | Mingyu Zhang[2] | Hongfei Wang[1] | Yong Hu[2]

[1]Zhejiang Key Laboratory of Advanced Catalysis and Adsorption Materials, Key Laboratory of the Ministry of Education for Advanced Catalysis Materials, Department of Chemistry, Zhejiang Normal University, Jinhua, China | [2]Institute of Nanocatalysis and Energy Conversion, College of Chemistry and Materials Engineering, Zhejiang A&F University, Hangzhou, China

Correspondence: Hongfei Wang (whf0614@zjnu.edu.cn) | Yong Hu (yonghu@zafu.edu.cn)

Received: 31 July 2026 | **Revised:** 12 September 2026 | **Accepted:** 18 September 2026

Keywords: anion-affinitive ZIF-8 core | hydrophilic SiO_2 shell | interfacial protective layer | Zn anode | Zn-I_2 batteries

ABSTRACT

Aqueous zinc batteries are plagued by dendrite growth and parasitic reactions, calling for a rational interfacial design. Herein, we construct a core–shell ZIF-8@SiO_2 architecture on the Zn anode (ZFSI@Zn) via a self-nucleation route. The hydrophilic SiO_2 shell and anion-affinitive ZIF-8 core synergistically facilitate Zn^{2+} desolvation and transport, enhancing the 3D diffusion contribution while effectively suppressing interfacial concentration polarization. Consequently, the ZFSI@Zn anode delivers an extended lifespan of 1800 h at 1 mA cm^{-2}/1 mAh cm^{-2} and maintains remarkable stability even at an ultrahigh current density of 50 mA cm^{-2}. Beyond anode protection, strong SO_4^{2-} adsorption confers a negative surface charge that electrostatically repels I_3^-, thereby eliminating the shuttle effect in Zn-I_2 batteries. This enables a maximum specific capacity of 202.3 mAh g^{-1} at 0.2 A g^{-1} and an outstanding capacity retention of 89.8% over 65 000 cycles at 5 A g^{-1}, corresponding to an ultralow capacity decay of merely 0.00015% per cycle. The superior performance is further validated under high cathode loadings and in pouch-cell configurations. Overall, this work establishes core–shell interfacial engineering as a versatile platform for tackling the multiple challenges in zinc-based energy storage.

1 | Introduction

The relentless surge in global electricity consumption, driven by the ongoing wave of electrification, has accentuated the pressing need for energy storage technologies that deliver both intrinsic safety and enduring operational reliability [1, 2]. While Li-ion batteries currently represent the state-of-the-art electrochemical storage solution, benefiting from superior energy densities and prolonged cycling stability, their large-scale implementation is severely hampered by several intrinsic drawbacks, including the flammability of organic electrolytes, the geopolitical and economic constraints associated with critical raw materials, and non-negligible safety hazards [3, 4]. Zn-ion batteries (ZIBs) present a compelling alternative for next-generation energy storage, leveraging the inherent safety of aqueous electrolytes, the earth Zn abundance, and a high theoretical capacity (820 mAh g^{-1} and 5855 mAh cm^{-2}) [5, 6]. While these attributes make ZIBs highly attractive for grid-scale applications, the reality is that their practical viability is severely constrained by deleterious phenomena at the Zn anode. Specifically, non-uniform Zn deposition leads to dendritic growth, which can breach the separator and cause catastrophic short circuits [7]. Simultaneously, the parasitic hydrogen evolution reaction (HER), surface corrosion, and insulating byproduct accumulation not only diminish the

All rights reserved, including rights for text and data mining and training of artificial intelligence technologies or similar technologies.
© 2026 Wiley-VCH GmbH

Coulombic efficiency (CE) but also create a positive feedback loop that accelerates dendrite propagation [8–10]. To overcome these obstacles, it is essential to devise rational strategies that can guide uniform Zn nucleation and growth while effectively mitigating interfacial side reactions.

Considerable efforts have been devoted to overcoming these obstacles, ranging from electrolyte engineering and separator functionalization to interfacial design [11, 12]. Among these approaches, the deliberate construction of a protective interphase layer on the Zn anode surface via interfacial regulation has garnered substantial attention, and has been unequivocally validated as an effective means of bolstering the electrochemical reversibility of Zn anodes [13, 14]. Conductive coatings (e.g., Sn [15], In [16], CuZn [17]) and insulating coatings (e.g., ZrO_2 [18], $CaCO_3$ [19], polyaniline [20]) have been developed as protective layers, each offering distinct advantages in regulating Zn nucleation and suppressing side reactions [21]. While conductive coatings reduce the nucleation barrier via zincophilic interactions, they inevitably leave the deposited Zn in direct contact with the electrolyte, rendering it vulnerable to parasitic corrosion [22]. Insulating coatings, on the other hand, serve as effective physical barriers against electrolyte attack, yet their intrinsically low ionic conductivity often leads to sluggish Zn^{2+} transport and consequent nonuniform deposition underneath the layer. The aforementioned limitations highlight the need for next-generation interfacial layers that can synergistically promote Zn^{2+} desolvation, ensure a uniform ionic flux, and maintain structural integrity during prolonged electrochemical operation [23, 24]. In this regard, the rational design of hierarchical architectures, which decouple the requirements of ionic transport and chemical shielding into distinct functional components, represents a promising pathway toward achieving long-lasting and highly reversible Zn anodes [25].

Beyond compositional considerations, the morphological order and structural integrity of the protective layer are equally crucial aspects that remain insufficiently investigated [26–28]. In particular, a well-ordered porous framework can be highly effective in accelerating the desolvation of hydrated Zn^{2+} ions. This kinetically retarded process precedes electrodeposition, and the framework facilitates it by confining ion migration within organized channels that promote the breakdown of the solvation sheath [29]. Simultaneously, such an ordered structure can sustain uninterrupted pathways for rapid ion migration, mitigating concentration polarization, and ensuring uniform Zn^{2+} flux toward the electrode surface [30, 31]. In sharp contrast, coatings with irregular or dense morphologies suffer from compromised ion accessibility and gradual structural degradation, leading to deteriorated performance and eventual device failure [32–34]. Hence, the deliberate construction of an interfacial layer with ordered morphology and built-in ion-regulation functionality is of paramount significance for achieving reversible, long-span Zn anode chemistry [35, 36].

In this work, we synthesized a core–shell ZIF-8@SiO_2 coating via a self-nucleation growth mechanism to stabilize the Zn anode (denoted as ZFSI@Zn). The outer inert SiO_2 shell effectively preserves the structural integrity of the inner ZIF-8 layer in the aqueous electrolyte environment. Beyond this protective function, the hierarchical layers serve a decoupling role. The SiO_2 shell exhibits hydrophilic properties, while the ZIF-8 core shows an affinity for anions, synergistically promoting the desolvation of hydrated Zn^{2+} ions and facilitating ion transport by decoupling them from coordinated water and SO_4^{2-}. Owing to this tailored interfacial regulation, the contribution of 3D diffusion during ion transport is enhanced, while concentration polarization at the interface is markedly alleviated, ensuring stable anode operation even under high-rate electrochemical conditions. Consequently, the ZFSI@Zn anode delivers exceptional performance, including an extended plating/stripping lifespan of 1800 h at 1 mA cm^{-2}/1 mAh cm^{-2} and robust stability at an ultrahigh current density of 50 mA cm^{-2}. Moreover, the effective adsorption of SO_4^{2-} renders the coating surface negatively charged, which suppresses the I_3^- shuttle effect in assembled Zn-I_2 batteries, leading to outstanding cycling performance under both high cathode loadings and pouch cell configurations. These results highlight that constructing a stable core–shell framework for ordered Zn^{2+} flux and rapid diffusion provides an efficient strategy for improving Zn anode performance, offering new insights into surface engineering for aqueous Zn-based batteries.

2 | Results and Discussion

The fabrication protocol for the designed electrodes and the associated interfacial regulation mechanism are schematically illustrated in Figure 1a. The ZFSI core–shell nanoparticles were synthesized via a self-nucleation growth mechanism. Specifically, ZIF-8 nanocrystals rapidly nucleated and grew when 2-methylimidazole (2-MI) and $Zn(NO_3)_2{\cdot}6H_2O$ were simultaneously introduced into the aqueous solution. Subsequently, the hydrolysis of tetraethyl orthosilicate (TEOS) was readily initiated on the surface of the pre-formed ZIF-8 particles. As shown in Figure S1, digital photographs of the bare Zn foil and the ZFSI@Zn electrode were acquired under identical lighting conditions. The ZFSI@Zn electrode exhibits a uniformly pale white coating across the entire surface, confirming the macroscopic homogeneity of the spin–coated ZFSI layer. The macroscopic uniformity of the coating is critical for ensuring consistent electrochemical performance across the entire electrode area and preventing localized dendrite formation or corrosion at uncoated regions [37]. The cross-sectional scanning electron microscopy (SEM) image shows that the ZFSI coating possesses a highly uniform thickness of approximately 22.5 μm and maintains intimate contact with the underlying Zn substrate, free from any visible gaps, delamination, or cracks (Figure S2). This excellent interfacial adhesion confirms that the spin–coating method yields a highly reproducible and homogeneous protective layer free of macroscopic defects. Attenuated total reflectance Fourier transform infrared spectroscopy (ATR-FTIR) of the sample obtained at the initial stage of the mixed stirring process reveals the emergence of Zn—OH vibrational bands alongside the characteristic peaks of ZIF-8 (Figure S3), confirming that the hydrolysis of TEOS occurred in a targeted and precise manner on the ZIF-8 surface [38]. This surface-induced precipitation process inherently serves as a critical step for the preparation of the composite without the need for any surfactant. Upon subsequent condensation and polymerization, high-purity ZFSI material was successfully obtained. SEM imaging shows that the as-obtained ZFSI product exhibits a spherical morphology (Figure 1b). X-ray diffraction (XRD) patterns confirm that the ZFSI composite

16163028, 2026, 89, Downloaded from https://advanced.onlinelibrary.wiley.com/doi/10.1002/adfm.78682 by Lei Li - Zhejiang Normal University , Wiley Online Library on [10/11/2026]. See the Terms and Conditions (https://onlinelibrary.wiley.com/terms-and-conditions) on Wiley Online Library for rules of use; OA articles are governed by the applicable Creative Commons License

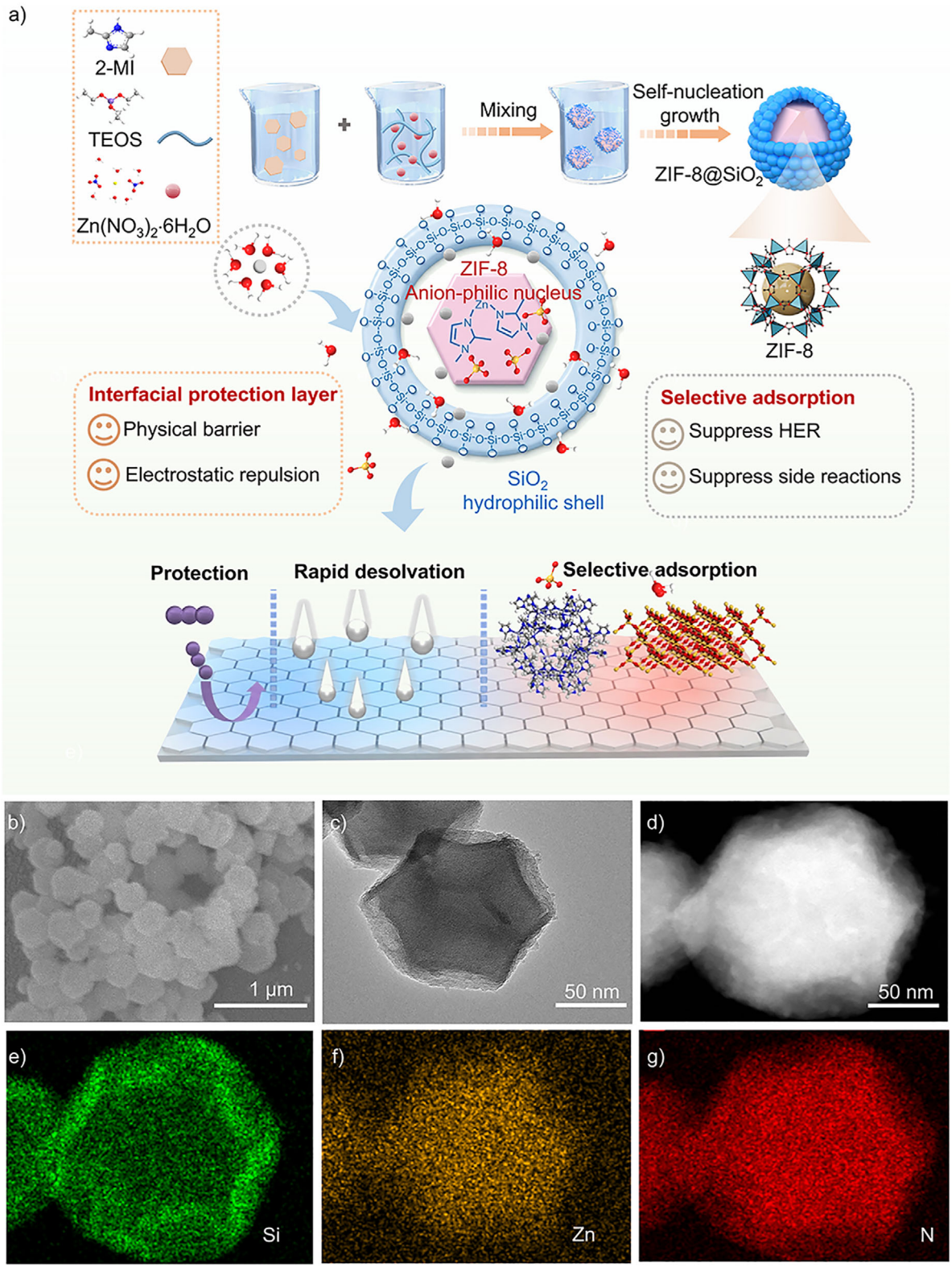

FIGURE 1 | (a) Schematic illustration of the self-nucleation growth mechanism for the preparation of core–shell ZFSI and its function in regulating Zn anode electrochemistry. (b) SEM and (c) TEM images of the ZFSI nanoparticles. (d) STEM image and corresponding elemental mapping of (e) Si, (f) Zn, and (g) N for a single ZFSI nanoparticle.

16163028, 2026, 89, Downloaded from https://advanced.onlinelibrary.wiley.com/doi/10.1002/adfm.78682 by Lei Li - Zhejiang Normal University , Wiley Online Library on [10/11/2026]. See the Terms and Conditions (https://onlinelibrary.wiley.com/terms-and-conditions) on Wiley Online Library for rules of use; OA articles are governed by the applicable Creative Commons License

retains the intact crystalline structure of ZIF-8, demonstrating the stable existence of the ZIF-8 framework within the hybrid architecture (Figure S4). ATR-FTIR spectroscopy further verifies the successful synthesis of ZFSI, with an absorption peak at 425 cm^{-1} corresponding to the Zn—N bond vibration of ZIF-8, and peaks at 1080 and 950 cm^{-1} attributable to the Si—O—Si stretching and Si—OH bending vibrations of SiO_2, respectively (Figure S5) [39]. X-ray photoelectron spectroscopy (XPS) was utilized to investigate the elemental composition of ZFSI. The survey spectrum confirms the presence of all characteristic elemental signatures originating from both SiO_2 and ZIF-8, corroborating the successful formation of the hybrid material (Figure S6a). The N 1s spectrum exhibits the characteristic Zn—N signature (Figure S6b), confirming the preservation of the ZIF-8 framework [40]. Meanwhile, the O 1s (Figure S6c) and Si 2p (Figure S6d) spectra display the typical Si—O bonds, attesting to the successful coupling of SiO_2 with ZIF-8 [41]. More significantly, the emergence of a Zn—O bonding signal points to interfacial chemical interactions between the Zn^{2+} sites of ZIF-8 and the SiO_2 component, which further substantiates that the self-nucleation of ZIF-8 serves as a platform for the subsequent growth of the SiO_2 shell. The mass ratio of ZIF-8 to SiO_2 in the ZFSI composite was determined by thermogravimetric analysis (TGA). The TGA curve presents a weight loss of approximately 33.2% for the ZIF-8 core and 62.4% for the SiO_2 shell, corresponding to a ZIF-8/SiO_2 mass ratio of approximately 0.53:1 (Figure S7).

Transmission electron microscopy (TEM) was employed to track the entire reaction and structural evolution process from the precursors to the final ZFSI nanoparticles. Within the initial 10 min, typical rhombic dodecahedral ZIF-8 nanocrystals nucleated and underwent rapid growth (Figure S8). As the reaction proceeded to 30 min, a core–shell structure featuring a spherical outer morphology was observed. Upon extending the reaction to 60 min, the ZFSI nanoparticles retained a rhombic dodecahedral morphology, with the SiO_2 shell thickness maintained at approximately 20 nm (Figure 1c). Scanning transmission electron microscopy (STEM) was further performed to elucidate the compositional distribution, which distinctly resolved the contrast difference between the ZIF-8 core and the SiO_2 shell (Figure 1d). In addition, energy-dispersive spectroscopy (EDS) elemental mapping was performed on a selected single ZFSI nanoparticle, revealing that Si is predominantly concentrated in the shell region, whereas Zn and N are mainly localized in the core (Figure 1e–g). This distinct elemental distribution provides direct evidence for the successful construction of the core–shell architecture. The microstructure and porosity of ZFSI were evaluated by N_2 adsorption-desorption measurements. The composite exhibits a typical type IV isotherm with a distinct hysteresis loop, indicative of mesoporous characteristics (Figure S9). The Brunauer-Emmett-Teller (BET) specific surface area and total pore volume were determined to be 640 $m^2\ g^{-1}$ and 0.32 $cm^3\ g^{-1}$, respectively. The corresponding pore size distribution further corroborates the presence of hierarchical porosity. Such a porous architecture is expected to facilitate electrolyte penetration into the electrode and provide efficient pathways for rapid ion transport [42].

The functionality of this core–shell interphase layer was investigated by using molecular dynamics (MD) simulations, density functional theory (DFT) calculations, and a range of electrochemical/spectroscopic characterizations. Through MD simulations, we directly compared the Zn^{2+} solvation configurations and the distribution profiles of SO_4^{2-} and H_2O at the electrode/electrolyte interfaces with and without the ZFSI layer (Figure 2a,b), unveiling the differential permeation dynamics and preferential transport pathways of ionic/molecular species across the modified interface. Quantitative insights derived from radial distribution function *g(r)* and coordination number *N(r)* analyses confirm that the presence of ZFSI reduces the coordination number of H_2O molecules in the hydrated Zn^{2+} shell from 5.15 to 4.64 and concomitantly decreases the coordinated SO_4^{2-} count from 0.85 to 0.78 (Figure 2c,d). The reduction in coordination number reflects the active involvement of the ZFSI framework in modifying the solvation environment through specific intermolecular interactions that weaken the original Zn^{2+}—H_2O and Zn^{2+}—SO_4^{2-} bonds, thereby facilitating the removal of coordinated species from the primary solvation sheath [43]. These findings suggest that the ZFSI framework possesses specific functional sites that actively reprogram the Zn^{2+} solvation shell by weakening Zn—H_2O interactions while restricting anion proximity, thus fostering a more favorable interfacial chemical environment for subsequent electrochemical reactions. To gain deeper insight into the functional differentiation within the ZFSI core–shell structure, we examined the relative density distributions of SO_4^{2-} and H_2O. Radial distribution profiles reveal a distinct spatial segregation: H_2O preferentially accumulates in the outer SiO_2 shell, while SO_4^{2-} is enriched in the inner ZIF-8 core (Figure 2e). This asymmetric distribution implies that the SiO_2 shell exhibits a strong affinity for water, whereas the ZIF-8 core selectively binds SO_4^{2-} anions. DFT calculations were subsequently employed to verify these proposed interactions. The binding energy data confirm that SiO_2 interacts with H_2O (−2.83 eV) much more strongly than ZIF-8 (−2.21 eV) does, underscoring the dehydration-promoting role of the outer shell (Figure 2f). Meanwhile, the significantly higher binding energy between ZIF-8 and SO_4^{2-} (−3.55 eV) relative to SiO_2 and SO_4^{2-} (−3.11 eV) validates the core's preferential anion sequestration (Figure 2g). In support of the above computational predictions, experimental spectroscopic evidence was also obtained. The Raman spectra in Figure 2h resolve the —OH stretching region (3000–3700 cm^{-1}) into three distinct components corresponding to strong, medium, and weak hydrogen bonds [44]. When the ZFSI coating is introduced, the interfacial water network exhibits a decreased fraction of both strong and weak hydrogen bonds and an increased fraction of medium hydrogen bonds compared with the bulk electrolyte, indicating the active role of hydrophilic SiO_2 in modulating water structure [45]. In addition, ATR-FTIR reveals that the SO_4^{2-} absorption peak in the ZFSI coating exhibits a pronounced red shift relative to that in the bulk electrolyte (Figure S10), attributable to the strong adsorptive affinity of the ZFSI framework toward SO_4^{2-} [46].

Given the demonstrated selective interactions of the ZFSI coating with electrolyte components, temperature-dependent electrochemical impedance spectra (EIS) measurements were performed on symmetric cells (Figure S11), and the resulting data were fitted according to the Arrhenius equation to extract the desolvation activation energy (E_a). As presented in Figure 2i, the ZFSI@Zn system exhibits a lower E_a value of 17.3 kJ mol^{-1} compared with 21.6 kJ mol^{-1} for the bare Zn electrode, indicating that the functional coating accelerates the dehydration step and furnishes a favorable kinetic foundation for rapid Zn^{2+} migration

16163028, 2026, 89, Downloaded from https://advanced.onlinelibrary.wiley.com/doi/10.1002/adfm.78682 by Lei Li - Zhejiang Normal University , Wiley Online Library on [10/11/2026]. See the Terms and Conditions (https://onlinelibrary.wiley.com/terms-and-conditions) on Wiley Online Library for rules of use; OA articles are governed by the applicable Creative Commons License

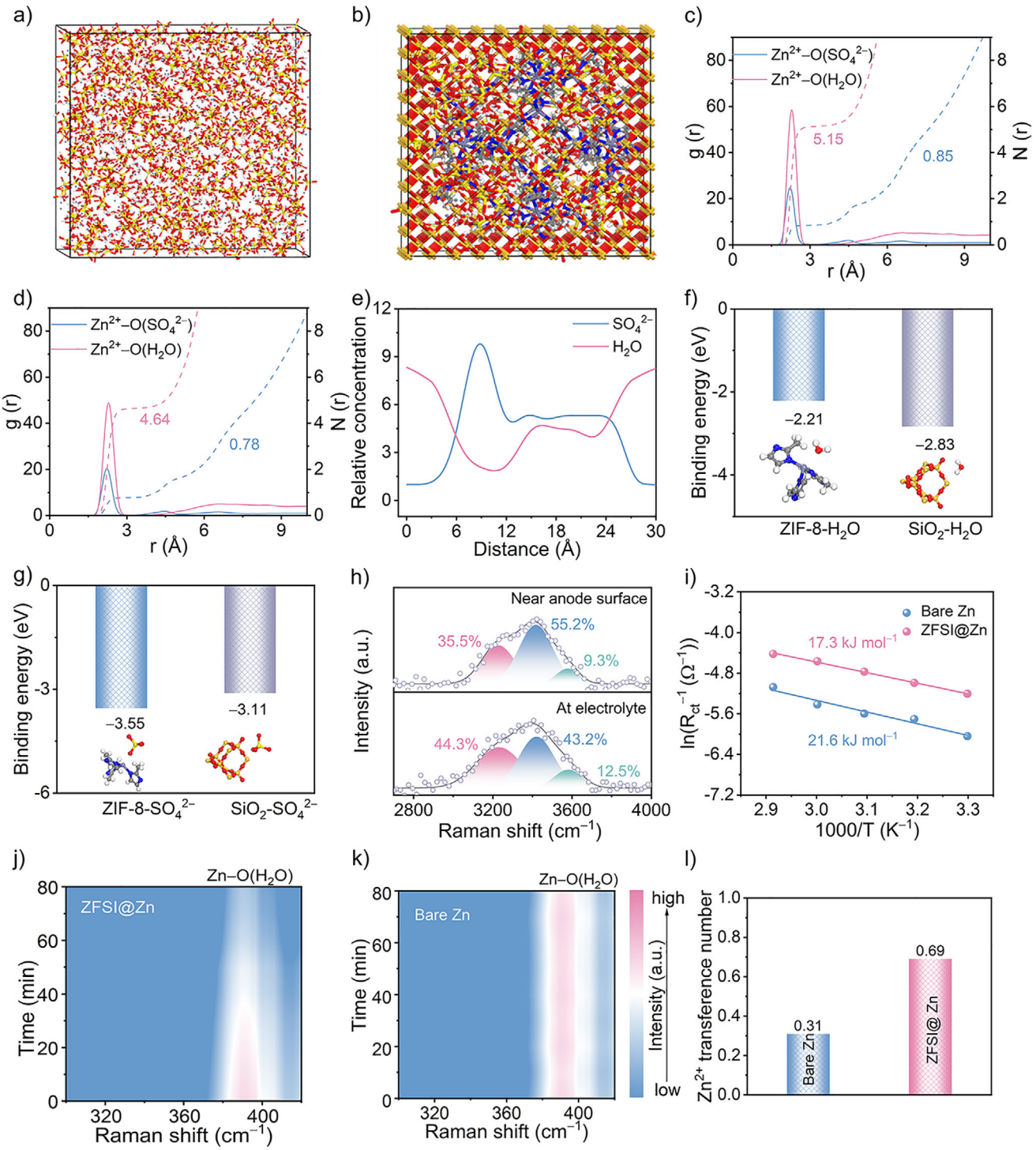

FIGURE 2 | 3D snapshots of MD simulations for (a) $ZnSO_4$ electrolyte and (b) electrolyte within ZFSI internal channels. Radial distribution functions of Zn^{2+}—$O(H_2O)$ and Zn^{2+}—$O(SO_4^{2-})$ from MD simulations for (c) bulk electrolyte and (d) ZFSI internal channels. (e) Density distribution profiles of SO_4^{2-} and H_2O inside the ZFSI channel. Binding energies of ZIF-8 and SiO_2 toward (f) H_2O and (g) SO_4^{2-} (insets: corresponding calculation models). (h) Raman spectra of the bulk electrolyte and the region near the ZFSI@Zn electrode, revealing distinct states of internal water molecules. (i) Activation energies derived from Nyquist plots of symmetric cells with different electrodes. In situ Raman spectroscopy monitoring the evolution of the Zn—$O(H_2O)$ stretching vibration at the (j) ZFSI@Zn and (k) bare Zn interfaces during electrodeposition. (l) Comparison of Zn^{2+} transference numbers across different electrodes.

16163028, 2026, 89, Downloaded from https://advanced.onlinelibrary.wiley.com/doi/10.1002/adfm.78682 by Lei Li - Zhejiang Normal University , Wiley Online Library on [10/11/2026]. See the Terms and Conditions (https://onlinelibrary.wiley.com/terms-and-conditions) on Wiley Online Library for rules of use; OA articles are governed by the applicable Creative Commons License

and subsequent homogeneous deposition. To directly probe the desolvation behavior of hydrated Zn^{2+} ions during electrodeposition, in situ Raman spectroscopy was performed by tracking the Zn—O(H_2O) stretching vibration at ~390 cm^{-1}, which is characteristic of the primary solvation sheath of $[Zn(H_2O)_6]^{2+}$ [47]. At the ZFSI@Zn interface, the intensity of this vibrational feature progressively declined upon the onset of deposition at 5 mA cm^{-2}, evidencing an efficient and expeditious desolvation process facilitated by the core–shell architecture (Figure 2j). The bare Zn electrode interface retained a pronounced signal attributable to the solvated species under identical conditions, reflecting markedly inferior desolvation kinetics (Figure 2k). Beyond the desolvation kinetics, the Zn^{2+} transference number was also evaluated via current-time (*I–t*) and EIS measurements on symmetric cells with/without ZFSI coating (Figure S12). The data in Figure 2l show that the ZFSI@Zn system achieves a higher Zn^{2+} transference number of 0.69, far exceeding the bare Zn value of 0.31. This increase confirms that the ZFSI layer greatly enhances Zn^{2+} mass transport, which is critical for sustaining rapid ion migration and maintaining interfacial stability under high-rate conditions [48–50].

The synergistic effects of the core–shell structure and internal chemical composition of the coating layer on Zn plating/stripping behavior were systematically investigated using symmetric cells. To assess the structural and compositional superiority of ZFSI in governing the Zn anode reactions, the pristine ZIF-8 counterpart without SiO_2 encapsulation, which exhibits a rhombic dodecahedral morphology (Figure S13), was similarly fabricated as a surface coating, and the resultant electrode is designated as ZF@Zn. Anode stability was first assessed by comparing voltage profiles obtained at a current density of 1 mA cm^{-2} and a fixed areal capacity of 1 mAh cm^{-2} (Figure S14). The bare Zn anode exhibits catastrophic failure at 55 h, as evidenced by erratic voltage behavior signaling internal short circuits. The ZF@Zn anode provides a marginal extension in service life to 270 h. By contrast, symmetric cells incorporating the ZFSI@Zn electrodes demonstrate exceptional voltage stability over the entire cycling period, achieving an operational lifetime of 1800 h, which corresponds to a 32.7-fold increase compared with that of the bare Zn anode. The long-term cycling performance of the Zn anodes is closely tied to the structural stability of the protective coatings in the battery environment. As shown in Figure S15, after 24 h of immersion in 2 M $ZnSO_4$ electrolyte, the pristine ZIF-8 particles suffered severe microstructural collapse: their characteristic dodecahedral shape was entirely lost and replaced by a loose architecture aggregated from numerous nanosheets, indicative of framework decomposition under acidic conditions. Impressively, the ZFSI coating remained essentially intact, with no observable corrosion or dissolution, underscoring the excellent chemical durability of the SiO_2 shell in the weakly acidic electrolyte and its effectiveness in preventing ZIF-8 degradation. ATR-FTIR spectroscopy was further employed to probe the structural stability of the different coatings before and after Zn plating/stripping cycling (Figure S16). The characteristic absorption peaks of ZFSI remained essentially unchanged after cycling, confirming that the coating preserved both its morphological integrity and internal compositional stability. Conversely, the ATR-FTIR spectra of the ZF@Zn electrode exhibited pronounced differences before and after cycling. Specifically, a new absorption band emerged at 3280 cm^{-1} (O—H stretching), indicative of hydrated water species on the anode surface. Meanwhile, strong bands at 1020 and 595 cm^{-1}, corresponding to the bending vibrations of SO_4^{2-}, confirmed the accumulation of sulfate species. Additionally, peaks at 760 and 1015 cm^{-1} were assigned to the characteristic vibrations of Zn—OH. Collectively, these spectral observations suggest that the ZIF-8 coating undergoes a substantial structural transformation during battery operation, yielding $Zn_4SO_4(OH)_6{\cdot}5H_2O$ [51]. The proposed transformation pathway is as follows: under attack by H^+ from the weakly acidic electrolyte, the Zn—N coordination bonds within the ZIF-8 framework are cleaved, and the 2-MI ligands are displaced by SO_4^{2-}. This intermediate subsequently reacts with $Zn(OH)_2$ formed in situ, ultimately affording $Zn_4SO_4(OH)_6{\cdot}5H_2O$. These results underscore that the core–shell architecture not only enables the synergistic regulation of the interfacial environment by its inner and outer components but also ensures robust structural integrity, thereby allowing ZFSI to sustain long-term efficacy during prolonged Zn plating/stripping processes. To rigorously verify the necessity of the ordered core–shell architecture, we further prepared Zn foils coated with pure SiO_2 (SI@Zn) and with a simple physical mixture of SiO_2 and ZIF-8 (ZF+SI@Zn). Symmetric cells employing these electrodes were then evaluated under demanding conditions of 10 mA cm^{-2} and 10 mAh cm^{-2}. The ZFSI@Zn symmetric cell not only maintains a stable voltage profile for approximately 610 h but also far surpassed the cycling durability of all comparative samples (Figure 3a). These results confirm that neither the physical mixture nor the individual components alone can replicate the performance of the core–shell structure, highlighting the critical importance of the spatially organized architecture for achieving the synergistic benefits in ion regulation and interfacial stabilization. A cross-sectional SEM image was taken of the ZFSI@Zn electrode after 50 cycles in a symmetric cell to evaluate the mechanical stability of the coating under prolonged electrochemical cycling. The interface between the coating and the Zn deposit remains clean and intimate, confirming that the coating maintains its mechanical integrity and protective function throughout extended cycling (Figure S17). More impressively, even when subjected to the exceptionally demanding combination of 50 mA·cm^{-2} and 5 mAh·cm^{-2}, the ZFSI@Zn cell sustains stable operation for 125 h without significant degradation (Figure 3b). To evaluate the practical viability of the ZFSI-protected Zn anode under deep cycling conditions, symmetric cell tests were performed using 10 μm Zn foil at a current density of 5 mA cm^{-2} and an areal capacity of 5 mAh cm^{-2}, corresponding to a DOD of 85.4% (Figure S18) [52]. Remarkably, the ZFSI@Zn anode maintains stable operation for 190 h under this exceptionally demanding regime, highlighting the robust protection afforded by the core–shell interfacial design. The superior performance of the ZFSI@Zn anode over the bare Zn and ZF@Zn counterparts arises from the synergistic integration of structural regulation and interfacial chemical stabilization. Specifically, the core–shell hierarchical architecture furnishes abundant functional sites that effectively modulate solvation structures, suppress dendritic Zn growth, and inhibit detrimental side reactions. This integrated design endows the ZFSI@Zn anode with superior interfacial robustness and rate capability, firmly establishing it as a compelling enabling platform for practically sustainable aqueous ZIBs.

The reversibility of Zn plating/stripping was further probed via CE measurements in asymmetric cells at 1 mA cm^{-2} and

16163028, 2026, 89, Downloaded from https://advanced.onlinelibrary.wiley.com/doi/10.1002/adfm.78682 by Lei Li - Zhejiang Normal University , Wiley Online Library on [10/11/2026]. See the Terms and Conditions (https://onlinelibrary.wiley.com/terms-and-conditions) on Wiley Online Library for rules of use; OA articles are governed by the applicable Creative Commons License

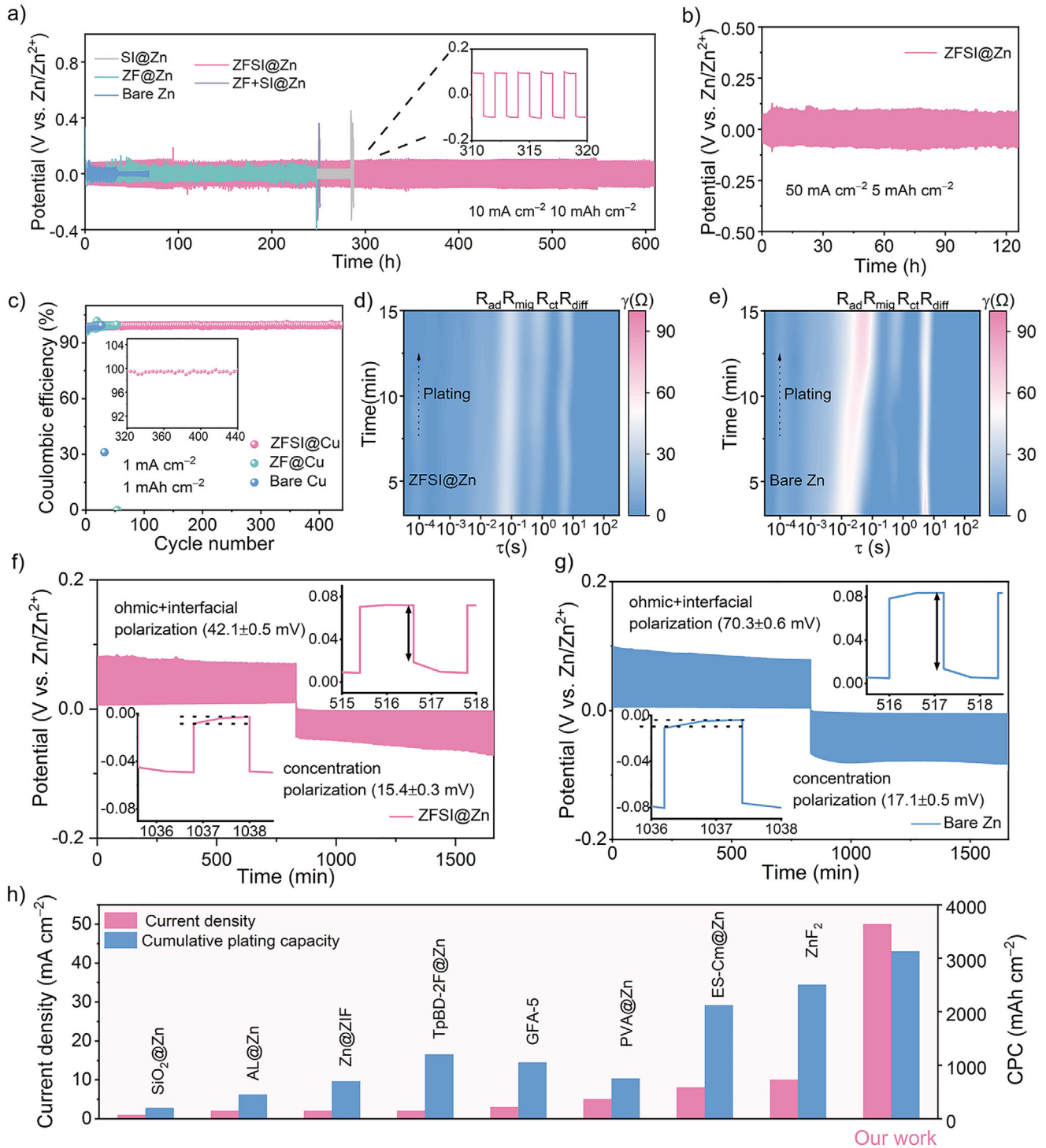

FIGURE 3 | Symmetric cell cycling at (a) 10 mA cm^{-2}/10 mAh cm^{-2} and (b) 50 mA cm^{-2}/5 mAh cm^{-2}. (c) CE of asymmetric cells at 1 mA cm^{-2}/1 mAh cm^{-2} (inset: CE test for the last 120 cycles). DRT contour maps from EIS of (d) ZFSI@Zn and (e) bare Zn during Zn deposition at 1 mA cm^{-2}. GITT curves of (f) ZFSI@Zn and (g) bare Zn symmetric cells with 1-min plating/stripping and 1-min rest at 1 mA cm^{-2} (insets: zoomed-in portions of the two GITT curves showing detailed potential responses during the intermittent steps). (h) CPC and current density of the ZFSI@Zn anode compared with other reported works.

1 mAh cm^{-2} (Figure 3c). A coated Cu electrode was used as the working electrode against a bare Zn foil counter/reference electrode. This design effectively circumvents interference from the intrinsic Zn reservoir, enabling a more reliable and accurate determination of the CE. The asymmetric cells based on bare Cu and ZF@Cu electrodes suffered rapid failure after merely 28 and 50 cycles, respectively, accompanied by severe CE fluctuations and pronounced voltage hysteresis. Such pronounced degradation arises from the activation of interfacial water molecules, which exacerbates the HER and triggers additional parasitic side reactions, alongside retarded Zn^{2+} desolvation and transport kinetics. These detrimental processes collectively

16163028, 2026, 89, Downloaded from https://advanced.onlinelibrary.wiley.com/doi/10.1002/adfm.78682 by Lei Li - Zhejiang Normal University , Wiley Online Library on [10/11/2026]. See the Terms and Conditions (https://onlinelibrary.wiley.com/terms-and-conditions) on Wiley Online Library for rules of use; OA articles are governed by the applicable Creative Commons License

accelerate uncontrolled Zn consumption, induce surface passivation, and promote highly localized plating/stripping behavior. Ultimately, these irreversible side reactions progressively destabilize the electrode interface and fundamentally constrain the long-term cycling reversibility. In stark contrast, the ZFSI@Cu-based asymmetric cell delivers markedly enhanced cycling stability, achieving an average CE of 99.3% over 440 cycles with consistently reversible voltage hysteresis (Figure S19). This superior reversibility is primarily attributable to the core–shell structured ZFSI coating, which effectively suppresses parasitic side reactions while simultaneously regulating Zn^{2+} transport kinetics at the electrode/electrolyte interface.

Beyond regulating Zn deposition, the stability and interfacial kinetics of the anode/electrolyte interface were further evaluated using in situ EIS combined with distribution of relaxation time (DRT) analysis in symmetric cells. As presented in Figure 3d,e, four distinct characteristic peaks of relaxation time (τ) were identified at approximately 0.01 s (τ_1), 0.1 s (τ_2), 1 s (τ_3), and 10 s (τ_4). These peaks are assigned to the adsorption/desolvation process (R_{ad}), surface migration process (R_{mig}), charge transfer process (R_{ct}), and Zn^{2+} diffusion process (R_{diff}), respectively [53]. Beyond the reduced τ_2 and τ_3 impedances signifying improved migration and charge transfer, the ZFSI@Zn anode presents a far more pronounced advantage at τ_1 and τ_4, where desolvation and diffusion impedances are drastically lowered. This compelling kinetic enhancement is unequivocally rooted in the synergistic coupling of the core–shell scaffold and the dual-component chemistry. The hydrophilic SiO_2 shell promotes Zn^{2+} desolvation by weakening Zn^{2+}—H_2O interactions, thereby lowering charge transfer resistance (reduced τ_3 peak). In adiition, the porous ZFSI framework facilitates rapid Zn^{2+} migration, effectively suppressing diffusion impedance (reduced τ_4 peak). Meanwhile, the coating suppresses parasitic side reactions and byproduct accumulation, preventing the interfacial degradation that typically increases impedance on bare Zn. These kinetic and chemical stabilization effects collectively outweigh the minor additional resistance from the coating layer, resulting in an overall lower impedance for the ZFSI@Zn electrode. The resulting cascade of benefits, including homogenized Zn^{2+} flux, mitigated ion aggregation, and suppressed dendrite incipiency, collectively ensures the sustained dendrite-free Zn deposition. To further elucidate the role of interfacial polarization in electrochemical performance, galvanostatic intermittent titration technique (GITT) measurements were conducted on symmetric cells [54]. The Zn plating/stripping process was performed in an intermittent mode at a current density of 1 mA cm^{-2}. The detailed testing protocol was as follows: the cell underwent a 1-min Zn plating step, followed by a 1-min open-circuit rest. Subsequently, a 1-min Zn stripping step was initiated, followed by a 1-min rest period. Statistical analysis was performed based on five segments of the potential curves (Figure S20). The results reveal that, owing to the efficient Zn^{2+} migration enabled by the core–shell coating channels, the concentration polarization voltage is reduced from 17.1 ± 0.5 to 15.4 ± 0.3 mV. Furthermore, the ohmic and interfacial polarization voltages are substantially suppressed, decreasing from 70.3 ± 0.6 mV for the bare Zn electrode to 42.1 ± 0.5 mV for the ZFSI@Zn electrode (Figure 3f,g). Collectively, the electrochemical test results corroborate that the ZFSI interfacial layer promotes efficient mass transport and significantly enhances the reversibility of Zn deposition/dissolution. It effectively overcomes the persistent challenges of poor kinetics, dendrite growth, and severe side reactions, laying a solid foundation for the advancement of next-generation ZIBs. As evidenced by Figure 3h and Table S1, the ZFSI@Zn anode achieves a high-rate capability of 50 mA cm^{-2} and an extended cumulative plated capacity (CPC) of 3125 mAh cm^{-2}, surpassing most previously reported Zn anodes with protective coatings. This comparison confirms that the synergy of ZFSI-based interfacial engineering and core–shell structural optimization offers a robust strategy to address the inherent instability of Zn metal anodes.

Given the exceptional plating/stripping reversibility, the Zn deposition behavior and the resultant surface chemistry were further scrutinized to elucidate the stabilizing effect of the functional interphase layer on the Zn anode. Upon approaching the anode, Zn^{2+} ions must undergo desolvation from their solvation sheath in the electrolyte, followed by surface diffusion on the electrode. This diffusion process typically proceeds through two sequential stages: initial 2D surface diffusion and subsequent 3D intracrystalline migration. The desolvated Zn^{2+} ions tend to undergo disordered 2D diffusion, driven by heterogeneous interfacial electric fields, which often results in loose and nonuniform deposition morphologies. If the interfacial architecture provides rapid 3D migration pathways, the duration of 2D diffusion can be substantially shortened, promoting an early transition to 3D diffusion and thereby enabling homogeneous and compact deposition. The core–shell framework featuring internal ZIF-8 and SiO_2 sites is expected to modulate the diffusion pathway of Zn^{2+} ions profoundly. The chronoamperometry (CA) profiles for the initial 60 s displayed in Figure S21 distinguish the diffusion kinetics on ZFSI@Zn from that on bare Zn. By fitting the CA current transients obtained from five parallel samples, three characteristic stages can be identified: double layer (DL), 2D instantaneous growth (2DI), and 3D instantaneous/progressive nucleation and growth (3DI/3DP) [55]. The fitting analyses indicate that while both electrodes exhibit instantaneous 3D nucleation, ZFSI@Zn drastically reduces the transition time from 2D to 3D diffusion to just 16.2 s, in stark contrast to 51.5 s for bare Zn (Figure 4a,b). Consistent results were obtained from the fitting of parallel samples (Figures S22 and S23). The proportion of the 3D diffusion stage on ZFSI@Zn reaches 72.7%±2.7% (Figure 4c), which is significantly higher than that on bare Zn (14.4%±1.6%), effectively alleviating the lateral accumulation of Zn nuclei. The 3D diffusion contribution represents the proportion of Zn^{2+} ions that follow an efficient, spatially distributed transport pathway through the porous coating channels, as opposed to disordered 2D surface diffusion. While the classical Scharifker–Hills model was developed for planar electrodes and assumes a homogeneous surface with no additional mass transport barriers, it remains a valuable comparative framework for evaluating deposition mechanisms. The porous coating may introduce additional ion transport pathways not fully captured by the model, and the presence of the coating may affect nucleation overpotential, active site density, and the nucleation mode. Nevertheless, the dramatic and reproducible difference in 3D diffusion contribution between bare Zn and ZFSI@Zn, together with complementary morphological and kinetic evidence, provides a consistent and meaningful indication of the fundamental change in deposition behavior enabled by the core–shell architecture. To probe the evolution of the ion concentration gradient during deposition, spatially resolved in situ Raman spectroscopy was applied to

16163028, 2026, 89, Downloaded from https://advanced.onlinelibrary.wiley.com/doi/10.1002/adfm.78682 by Lei Li - Zhejiang Normal University , Wiley Online Library on [10/11/2026]. See the Terms and Conditions (https://onlinelibrary.wiley.com/terms-and-conditions) on Wiley Online Library for rules of use; OA articles are governed by the applicable Creative Commons License

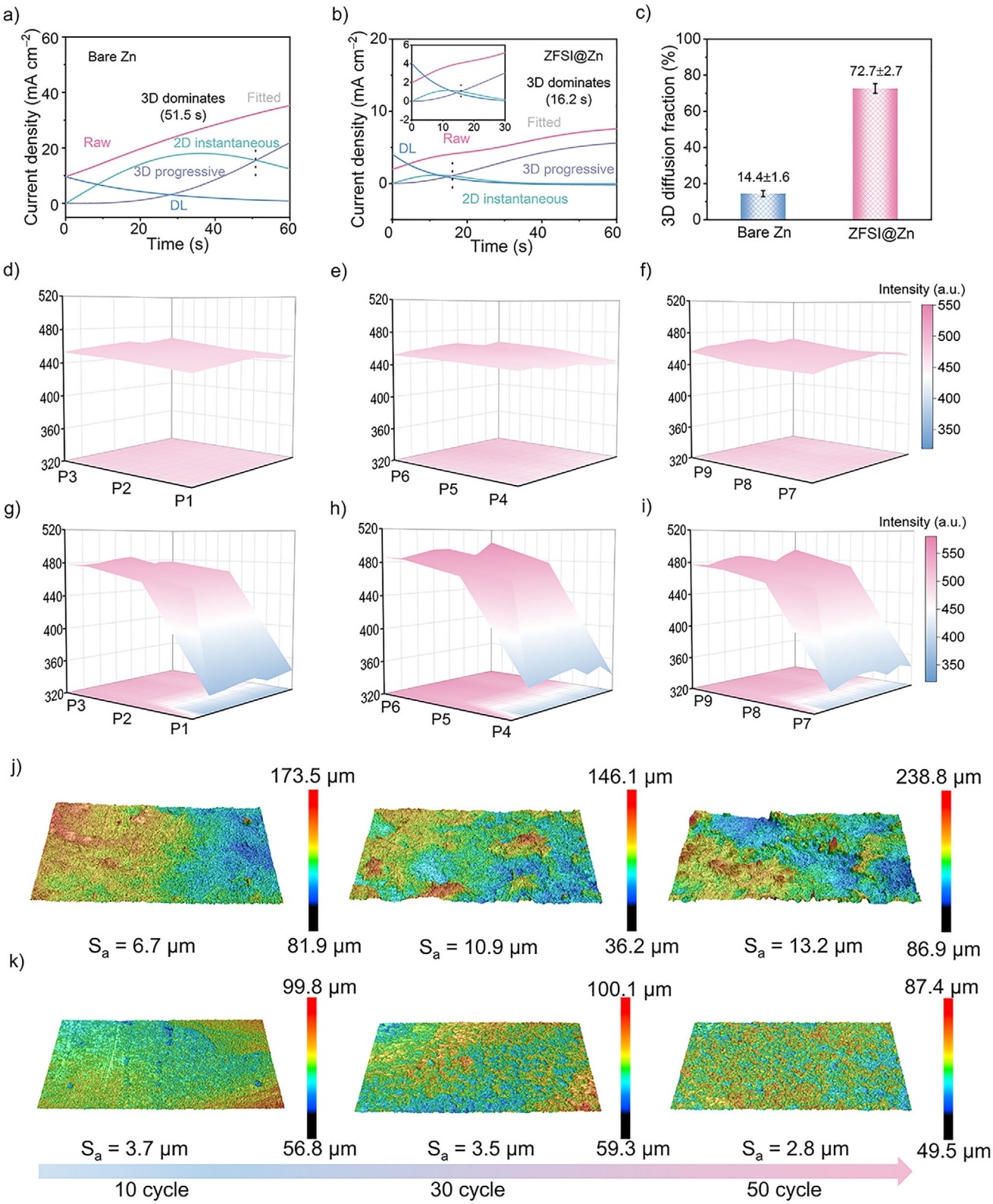

FIGURE 4 | CA curves of (a) bare Zn and (b) ZFSI@Zn recorded at an overpotential of −150 mV, along with (c) a quantitative comparison of the 3D diffusion contribution (inset of Figure 4b: magnified view of the CA fitting curve). Spatially resolved in situ Raman mapping of SO_4^{2-} concentration evolution at the (d–f) ZFSI@Zn interface during Zn electrodeposition, and (g–i) the corresponding analysis at the bare Zn interface. Ex situ CLSM images of (j) the bare Zn and (k) the ZFSI@Zn electrodes (coating removed) after different cycle numbers in symmetric cells.

16163028, 2026, 89, Downloaded from https://advanced.onlinelibrary.wiley.com/doi/10.1002/adfm.78682 by Lei Li - Zhejiang Normal University , Wiley Online Library on [10/11/2026]. See the Terms and Conditions (https://onlinelibrary.wiley.com/terms-and-conditions) on Wiley Online Library for rules of use; OA articles are governed by the applicable Creative Commons License

bare Zn and ZFSI@Zn. The test setup and point distribution are shown in Figure S24, with the SO_4^{2-} peak identified at 980 cm^{-1}. A total of nine sampling sites were defined in a 3 × 3 array within the electrolyte layer immediately adjacent to the working electrode [56]. Spectral acquisition was performed at three distinct vertical tiers relative to the electrode surface: the near-surface tier (P1, P4, and P7), the intermediate tier (P2, P5, and P8), and the bulk-electrolyte tier (P3, P6, and P9), enabling a comprehensive profile of concentration variations along the diffusion direction. The corresponding raw data can be found in Figures S25 and S26 and Tables S2 and S3. A comparative analysis of the SO_4^{2-} intensity distribution across the selected interfacial regions during Zn deposition manifests a striking dichotomy between the two electrodes. On the ZFSI@Zn surface, the SO_4^{2-} concentration is effectively preserved at a relatively constant level throughout the electrodeposition process (Figure 4d–f). This stabilization arises from the ion-regulation capability of the core–shell framework, which weakens the strong electrostatic coupling between Zn^{2+} and SO_4^{2-} in the solvation sheath. The energy barrier for Zn^{2+} desolvation is lowered, and the ionic migration pathway is streamlined, enabling a highly efficient and sustained 3D diffusion flux. At the bare Zn interface, the SO_4^{2-} signal undergoes a rapid and severe depletion (Figure 4g–i), signaling the onset of acute concentration polarization. This localized anion depletion establishes a substantial electric field gradient, which in turn drives erratic and nonuniform Zn^{2+} migration while promoting lateral adatom aggregation, a process that serves as a precursor to dendritic nucleation and subsequent proliferation. The sharp contrast between these two scenarios unequivocally demonstrates that the ZFSI interphase serves as an effective ionic modulator, not only alleviating concentration polarization but also orchestrating a homogeneous ionic distribution that is essential for dendrite-free deposition.

In addition, in situ optical microscopy was employed to dynamically track the nucleation and growth evolution of the Zn anode during electrodeposition. The experiment was conducted at a current density of 5 mA·cm^{-2}, and the surface morphology changes were continuously recorded throughout the deposition process. The bare Zn electrode exhibits visible dendritic deposits on its surface after only 40 min of electroplating (Figure S27). These dendritic features further evolve into sharp protruding tips during subsequent deposition, severely compromising the stability of the electrode interface. In stark contrast, for the ZFSI@Zn electrode, the surface maintains a dense and planar deposition morphology over the entire 60 min period [57]. Ex situ SEM imaging was performed on the Zn electrodes at different cycle numbers in symmetric cells at 10 mA cm^{-2} with an areal capacity of 10 mAh cm^{-2} to track the morphological evolution. Initially, nonuniform protrusions are observed after 10 cycles. These features then develop into randomly distributed agglomerates after 50 cycles, indicating severe interfacial degradation. In striking contrast, the ZFSI@Zn electrode maintains a consistently dense, smooth, and compact surface throughout the entire cycling process, with no signs of dendrites, cracking, or byproduct residues (Figure S28). Confocal laser scanning microscopy (CLSM) topographic analysis was conducted at the same cycling intervals to quantify the evolution of surface roughness. The bare Zn electrode exhibits a progressive increase in average surface roughness (S_a), with the S_a value rising from approximately 6.7 μm at 10 cycles to 13.2 μm at 50 cycles (Figure 4j). By contrast, the ZFSI@Zn electrode displays remarkably stable surface topography throughout cycling, with the S_a value decreasing modestly from approximately 3.7 μm at 10 cycles to 2.8 μm at 50 cycles (Figure 4k). These direct morphological observations indicate that the ZFSI coating effectively homogenizes Zn^{2+} flux, suppresses dendritic growth, and preserves interfacial stability during extended electrochemical operation. SEM images of the cycled electrodes presented in Figure S29 reveal that the bare Zn anode suffers from severe dendritic growth and abundant byproduct residues. In contrast, the underlying Zn surface of the ZFSI@Zn electrode, after removal of the coating, remains smooth and devoid of corrosion, confirming the effective suppression of side reactions and passivation enabled by the protective layer. The corresponding XRD patterns corroborate these morphological observations (Figure S30). The bare Zn anode features pronounced diffraction peaks indexed to the typical byproduct phase $Zn_4SO_4(OH)_6{\cdot}5H_2O$ (PDF #39-0688), indicating severe side reactions between the Zn surface and the electrolyte. The ZFSI@Zn electrode shows no detectable reflections from any byproduct phases, underscoring the ability of the protective interphase to effectively block the electrolyte penetration and suppress the precipitation of insulating Zn hydroxy sulfate species. The protective efficacy of the ZFSI layer toward the Zn anode was further evaluated by probing the interfacial side reactions using linear polarization (LP) and linear sweep voltammetry (LSV). Tafel results (Figure S31) show that the ZFSI@Zn electrode achieves a higher corrosion potential and lower corrosion current density (−0.028 V, 0.18 mA cm^{-2}) than bare Zn (−0.033 V, 1.33 mA cm^{-2}), confirming that the ZFSI coating effectively enhances corrosion resistance and reduces the corrosion rate of the Zn anode. The ZFSI exhibits a significantly lower water contact angle (36.3°) compared to bare Zn (89.5°) (Figure S32), indicating enhanced surface hydrophilicity. This improved wettability correlates with an increased interfacial free energy, consequently curtailing the HER-triggered corrosion. The HER activity at the Zn electrode surface was further investigated using LSV measurements. As depicted in Figure S33, the ZFSI@Zn electrode consistently exhibits a lower current density and a more negative HER onset potential (−0.204 V) compared with bare Zn (−0.077 V) at 10 mA cm^{-2}. This suppressed HER kinetics is attributed to the presence of hydrophilic SiO_2 components within the interphase layer, which effectively shield the solvated water molecules from polarization-induced decomposition. Taken together with the preceding analyses of deposition morphology, concentration polarization, and corrosion behavior, these findings affirm that the ZFSI interphase serves as a protective platform that not only regulates Zn^{2+} diffusion and nucleation but also suppresses parasitic reactions, thereby ensuring robust interfacial stability.

To evaluate the practical applicability of the ZFSI@Zn anode, full batteries were assembled using I_2-loaded nitrogen-doped carbon as the cathode (denoted as ZFSI@Zn//I_2), and their electrochemical performance was compared with that of bare Zn//I_2 cells. Cyclic voltammetry (CV) was carried out at a scan rate of 1 mV s^{-1} (Figure 5a), where a redox couple corresponding to the I^0/I^- transition is clearly resolved at 1.20 and 1.32 V. The polarization voltage gap for this couple is 120 mV in the ZFSI@Zn//I_2 battery, significantly outperforming the bare Zn//I_2 battery, which exhibits a much larger gap of 210 mV. To investigate the reaction kinetics of the full batteries, *b*-values were derived from CV measurements at various scan rates. As presented in Figure S34,

16163028, 2026, 89, Downloaded from https://advanced.onlinelibrary.wiley.com/doi/10.1002/adfm.78682 by Lei Li - Zhejiang Normal University , Wiley Online Library on [10/11/2026]. See the Terms and Conditions (https://onlinelibrary.wiley.com/terms-and-conditions) on Wiley Online Library for rules of use; OA articles are governed by the applicable Creative Commons License

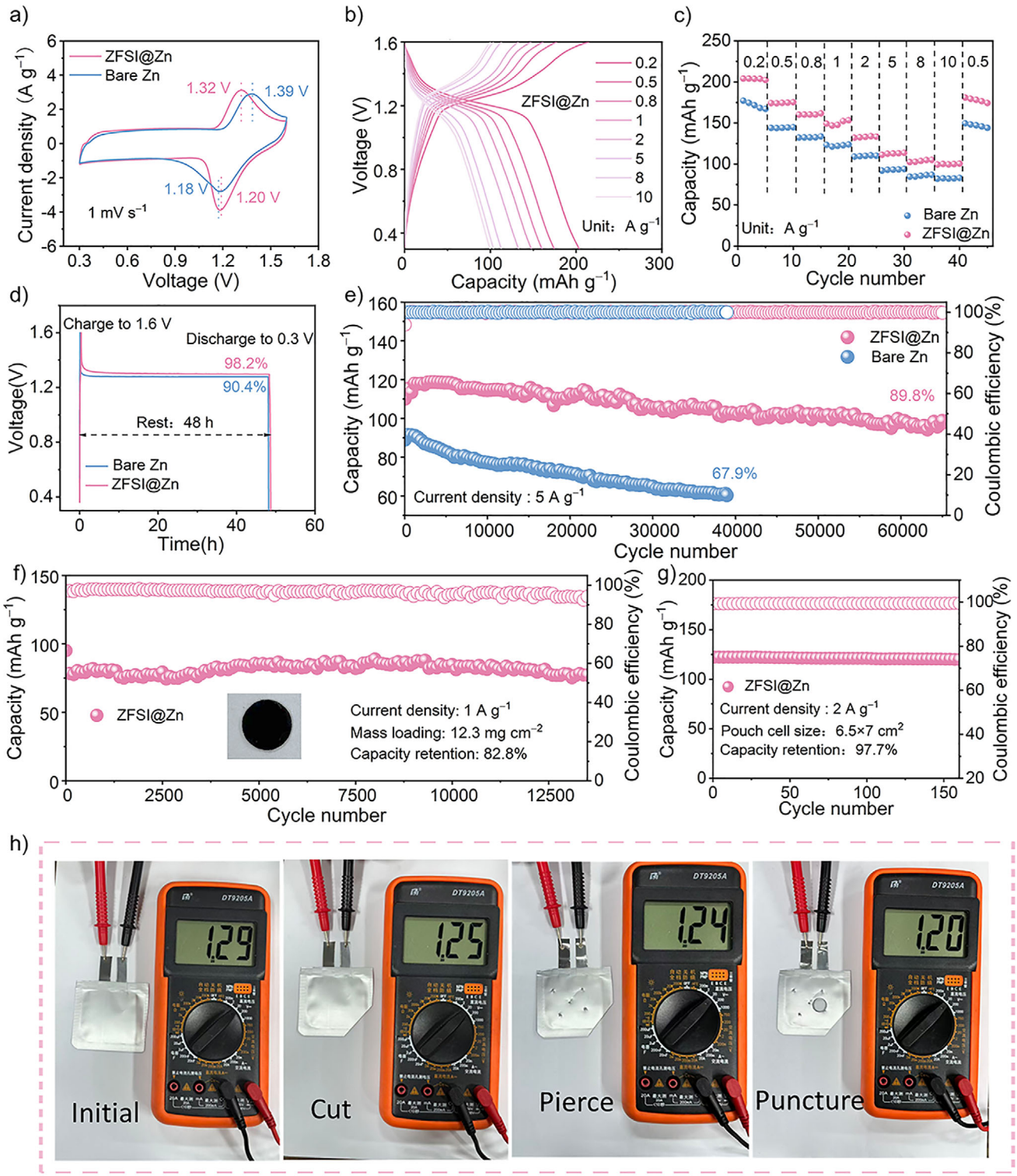

FIGURE 5 | (a) CV curves of ZFSI@Zn//I_2 and bare Zn//I_2 batteries at 1 mV s^{-1}. (b) GCD profiles of the ZFSI@Zn//I_2 battery under different current densities. (c) Rate performance. (d) Self-discharge tests of Zn//I_2 and ZFSI@Zn//I_2 batteries. (e) Long-term cycling performance of full batteries with different anodes at 5 A g^{-1}. (f) Cycling evaluation at a high mass loading of 12.3 mg cm^{-2} (inset: photograph of the cathode at this mass loading). (g) Cycling stability of the pouch-type cell at 2 A g^{-1}. (h) Open-circuit voltage and safety evaluation of the pouch-type cell under destructive mechanical conditions.

16163028, 2026, 89, Downloaded from https://advanced.onlinelibrary.wiley.com/doi/10.1002/adfm.78682 by Lei Li - Zhejiang Normal University , Wiley Online Library on [10/11/2026]. See the Terms and Conditions (https://onlinelibrary.wiley.com/terms-and-conditions) on Wiley Online Library for rules of use; OA articles are governed by the applicable Creative Commons License

the *b*-values of the ZFSI@Zn//I_2 full battery are consistently higher than those of the bare Zn//I_2 counterpart, indicating that the electrochemical process of the former is predominantly governed by surface-capacitive behavior, which enables faster pseudocapacitive reaction kinetics. EIS measurements in Figure S35 further confirm this interpretation, as the semicircle radius in the high-to-middle frequency region is smaller for the ZFSI@Zn electrode, reflecting a lower R_{ct} value at the electrode/electrolyte interface. This reduced interfacial resistance facilitates faster ion and electron transport, thereby contributing to the excellent high-rate performance of the ZFSI@Zn//I_2 full battery [58].

The galvanostatic discharge–charge (GCD) performance of the ZFSI@Zn//I_2 battery was evaluated over a current density range of 0.2 to 10 A g^{-1} (Figure 5b and Figure S36). The ZFSI@Zn//I_2 full battery not only maintains lower voltage polarization but also delivers higher specific capacities across all tested current densities. As shown in Figure 5c, the ZFSI@Zn//I_2 battery achieves a maximum specific capacity of 202.3 mAh g^{-1} at 0.2 A g^{-1}, while retaining a substantial capacity of 100.3 mAh g^{-1} even at a high current density of 10 A g^{-1}, underscoring its rapid reaction kinetics and excellent reversibility. In stark contrast, the bare Zn//I_2 battery delivers markedly lower capacities of only 177.1 and 82.6 mAh g^{-1} at 0.2 and 10 A g^{-1}, respectively. The enhanced rate capability is attributed to the ZFSI layer's ability to lower concentration polarization and charge-transfer resistance for faster kinetics, as well as its effective suppression of detrimental side reactions that typically degrade performance at high current densities. Moreover, self-discharge tests following a 48 h rest period (Figure 5d) demonstrate that the ZFSI@Zn//I_2 battery exhibits a superior capacity retention of 98.2%, compared with 90.4% for the bare Zn//I_2 battery. The significantly reduced capacity loss confirms that the ZFSI layer effectively mitigates parasitic side reactions during storage.

The long-term cycling performance of full batteries with different anodes is presented in Figure 5e. At a current density of 5 A g^{-1}, the battery incorporating the ZFSI@Zn anode retains 89.8% of its initial capacity after 65 000 cycles, with an ultralow capacity decay of only 0.00015% per cycle. This performance far surpasses that of the bare Zn anode-based battery, which achieves only 67.9% capacity retention after just over 38 000 cycles. To assess the structural integrity of the ZFSI coating under realistic operating conditions, SEM and XRD analyses were performed on the ZFSI@Zn electrode after 100 cycles in a full Zn-I_2 battery. The post-cycling SEM images reveal that the ZFSI coating largely maintains its initial spherical morphology and uniform coverage, with no visible microcracks, pinholes, or delamination (Figure S37). The XRD pattern confirms the preservation of the ZIF-8 framework without detectable byproduct formation (Figure S38). These results demonstrate that the SiO_2 shell provides durable mechanical and chemical protection, effectively preventing electrolyte penetration and maintaining the structural integrity of the core–shell architecture over extended operation. The superiority of the ZFSI-modified anode was further underscored under high-mass-loading conditions (Figure 5f). The battery retains 82.8% of its capacity after 13 000 cycles even at a high loading of 12.3 mg cm^{-2}. This exceptional stability is primarily attributed to the ZFSI layer's efficacy in curbing iodine shuttling, which prevents active material depletion and safeguards the electrode structure during long-term operation. Building upon the success in coin-cell configuration, we fabricated pouch-type batteries to assess their practical potential. The pouch cell delivers an initial specific capacity of 122.3 mAh g^{-1} and exhibits robust cyclability with 97.7% capacity retention over 160 cycles at 2 A g^{-1} (Figure 5g). Furthermore, the cell shows exceptional tolerance to severe mechanical damage: even under harsh conditions such as cutting, piercing, or puncturing, it maintains a stable open-circuit voltage without failure (Figure 5h). These results collectively affirm the feasibility and reliability of the ZFSI@Zn anode for demanding real-world applications.

To further probe the effectiveness of ZFSI in mitigating the polyiodide shuttle under static conditions, an H-type cell was set up with a Whatman glass fiber (GF) membrane serving as the separator. The left chamber was filled with a reddish-brown polyiodide solution (2 M $ZnSO_4$ + 0.05 M I_3^-), while the right chamber contained a colorless 2 M $ZnSO_4$ solution. As illustrated in Figure 6a, the right-chamber solution underwent a rapid color change from colorless to reddish-brown within 18 h when the pristine GF membrane was used, revealing that the bare separator offers no discernible barrier against polyiodide migration. When a ZFSI-modified GF membrane (ZFSI@GF) was used as the separator in the H-type cell, Figure 6b shows that the solution in the right chamber remained colorless and transparent even after 18 h. The pronounced difference originates from the adsorption of SO_4^{2-} ions onto the ZFSI coating, which renders the surface negatively charged. This mechanism is corroborated by zeta potential measurements, showing that the ZFSI surface becomes significantly more negative in 2 M $ZnSO_4$ electrolyte compared to deionized water (Figure S39). The resulting electrostatic field at the coating surface provides an effective electrostatic repulsion barrier, endowing the coating with superior blocking capability against the polyiodide shuttle. While the ZFSI@GF separator effectively suppresses polyiodide migration via electrostatic repulsion, its role is limited to shuttle inhibition. The ZFSI coating applied directly on the Zn anode provides dual functionality, as it electrostatically repels I_3^- at the anode interface while simultaneously promoting Zn^{2+} desolvation and facilitating rapid ion transport. The anode coating therefore offers a more comprehensive strategy for addressing the multifaceted challenges in Zn-I_2 batteries. To further unravel the underlying interactions between the SO_4^{2-}-bound ZFSI coating and polyiodide species, electrostatic potential (ESP) distribution calculations were performed. As shown in Figure 6c, the ESP analysis demonstrates that the I_3^- ion exhibits an overall negative charge with a surface electrostatic potential value of −1.16 eV. In line with the earlier discussion that the core–shell structured ZFSI immobilizes SO_4^{2-} through the functional sites of ZIF-8 during electrochemical reactions, the ESP results confirm that the SO_4^{2-}-bound ZFSI coating carries a negative surface charge (Figure 6d). Consequently, this electrostatic repulsion is expected to function as a physical barrier that prevents direct contact between polyiodide ions and the anode surface [59]. The exceptional capacity performance of the full battery is largely attributed to the ZFSI coating's effective suppression of the polyiodide shuttle effect. The strong adsorption of SO_4^{2-} endows the coating surface with a negative charge, which electrostatically repels the negatively charged I_3^- species. Consequently, the iodine species are effectively confined to the cathode compartment, preventing their migration toward the anode. This ensures that the

16163028, 2026, 89, Downloaded from https://advanced.onlinelibrary.wiley.com/doi/10.1002/adfm.78682 by Lei Li - Zhejiang Normal University , Wiley Online Library on [10/11/2026]. See the Terms and Conditions (https://onlinelibrary.wiley.com/terms-and-conditions) on Wiley Online Library for rules of use; OA articles are governed by the applicable Creative Commons License

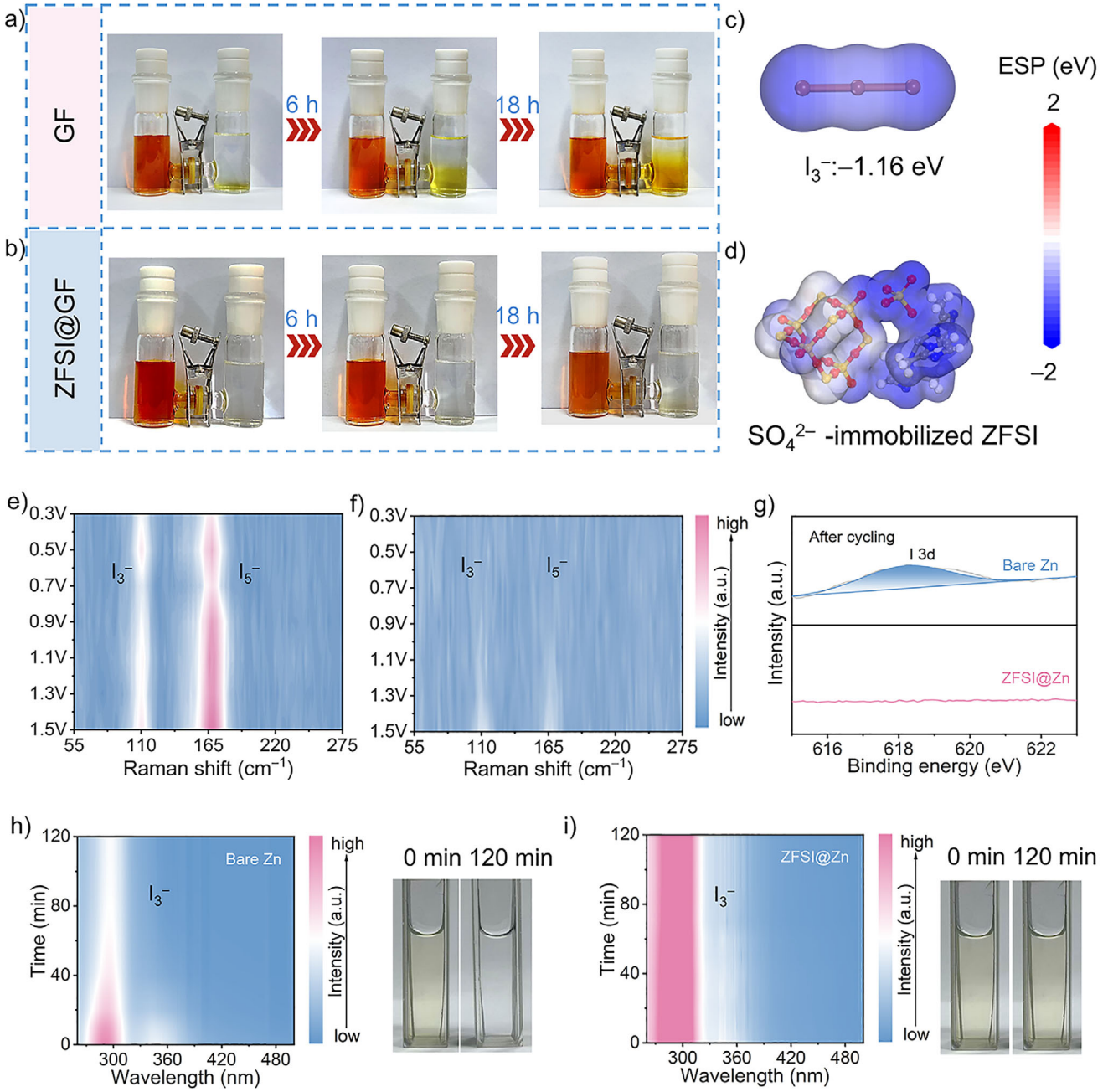

FIGURE 6 | Digital photographs of the H-type electrolytic cells with (a) GF and (b) ZFSI@GF separators after standing for different time intervals. ESP distribution of (c) I_3^- and (d) the SO_4^{2-}-immobilized ZFSI. In situ Raman spectra of the anode surfaces of (e) Zn//I_2 and (f) ZFSI@Zn//I_2 batteries during discharge. (g) I 3d XPS spectra of bare Zn and ZFSI@Zn anodes after cycling. In situ UV--vis absorption spectra of the bulk electrolytes for (h) bare Zn and (i) ZFSI@Zn tested in homemade symmetric cells.

overwhelming majority of I_2 is fully reduced via the two-electron redox process ($I_2 + 2e^- \rightarrow 2I^-$).

In situ Raman spectroscopy was employed to investigate the anti-corrosion performance of the ZFSI coating against polyiodide-induced Zn corrosion, by analyzing the anode surface of ZFSI@Zn//I_2 and Zn//I_2 batteries during discharge. Figure 6e presents that two characteristic peaks at 110 and 165 cm^{-1}, assignable to I_3^- and I_5^-, appear on the Zn//I_2 anode surface, evidencing polyiodide shuttling and consequent corrosion. In contrast, only a relatively small amount of polyiodide signatures is observed on the ZFSI@Zn//I_2 anode (Figure 6f), confirming that the interfacial layer effectively excludes polyiodides via electrostatic repulsion and protects the Zn anode from corrosion. SEM images acquired after electrochemical testing provide additional evidence for the protective function of the ZFSI coating. The ZFSI@Zn electrode exhibits a well-preserved smooth surface without obvious morphological alterations, whereas the bare Zn electrode suffered from a certain degree of surface damage, characterized by the emergence of some pits and craters (Figure S40). XPS I spectra collected from the cycled electrodes further substantiate the superior protection of the ZFSI coating: iodine species

16163028, 2026, 89, Downloaded from https://advanced.onlinelibrary.wiley.com/doi/10.1002/adfm.78682 by Lei Li - Zhejiang Normal University , Wiley Online Library on [10/11/2026]. See the Terms and Conditions (https://onlinelibrary.wiley.com/terms-and-conditions) on Wiley Online Library for rules of use; OA articles are governed by the applicable Creative Commons License

are clearly identified on the bare Zn anode, yet completely absent on the ZFSI@Zn anode (Figure 6g). In situ UV–vis absorption spectroscopy was carried out using a custom-built symmetric cell placed in a cuvette, with the electrolyte containing 2 M $ZnSO_4$ and 5 mM I_3^-. Upon cycling the Zn//Zn cell for 120 min, the UV–vis light was directed through the bulk electrolyte, and the resulting spectra are displayed in Figure 6h [60]. The characteristic peak of I_3^- at 286.9 nm shows a pronounced intensity decline from the initial state to 120 min. Concurrently, the accompanying optical images show that the electrolyte gradually fades from light yellow to nearly colorless. This spectral and visual evidence consistently demonstrates that the I_3^- species in the electrolyte are depleted via a chemical reaction with metallic Zn. Zn metal is particularly susceptible to severe corrosion caused by polyiodine species ($Zn + I_3^- \rightarrow Zn^{2+} + 3I^-$), resulting in poor CE and limited cyclability [61, 62]. In marked contrast, the symmetric cell equipped with ZFSI@Zn electrodes exhibits remarkably stable I_3^- signal intensity in the bulk electrolyte over 120 min, accompanied by negligible color change (Figure 6i). A ZFSI-coated I_2 cathode was also prepared by spin–coating a ZFSI slurry onto the I_2-loaded carbon paper electrode, which was then assembled into a full cell with a bare Zn anode. In situ UV–vis absorption spectroscopy was performed on the electrolyte collected from the cell during operation. Almost no detectable I_3^- absorption peaks were observed throughout the entire cycling process, with the UV–vis spectra remaining essentially flat and featureless (Figure S41). This result similarly confirms that the ZFSI coating effectively suppresses the shuttle effect by electrostatically repelling the anionic I_3^- species. It should be noted that while the ZFSI coating on the cathode effectively suppresses shuttle, it does not address the challenges at the Zn anode, such as dendrite growth and parasitic side reactions. For practical applications where both anode and cathode stability are required, the anode coating remains the more comprehensive solution, as it simultaneously addresses Zn^{2+} desolvation, ion transport, dendrite suppression, and shuttle inhibition. Therefore, these observations unequivocally confirm that the ZFSI coating effectively protects the Zn anode from I_3^- corrosion, affording the ZFSI@Zn//I_2 full battery with highly reversible iodine redox reactions and superior long-term cycling stability.

3 | Conclusion

In summary, we have developed a core–shell ZFSI coating via a self-nucleation route to stabilize Zn anodes. Functionally, the two components work in a complementary decoupling manner: the hydrophilic SiO_2 shell and the anion-philic ZIF-8 core collaboratively facilitate the desolvation of hydrated Zn^{2+} ions and accelerate ion transport by stripping coordinated water and SO_4^{2-} from the solvation sheath. The 3D diffusion contribution is substantially enhanced and interfacial concentration polarization is markedly alleviated, thereby ensuring stable anode operation under high-rate conditions. Benefiting from these merits, the ZFSI@Zn anode achieves an impressive lifespan of 1800 h at 1 mA cm^{-2}/1 mAh cm^{-2} and maintains excellent stability even at an ultrahigh current density of 50 mA cm^{-2}. More importantly, the negatively charged coating surface, arising from its strong adsorption toward SO_4^{2-}, effectively immobilizes I_3^- species and suppresses the shuttle effect. As a result, the Zn-I_2 battery delivers a maximum capacity of 202.3 mAh g^{-1} and exhibits extraordinary cycling durability with 89.8% capacity retention after 65 000 cycles at 5 A g^{-1}, corresponding to an ultralow capacity decay of only 0.00015% per cycle. Furthermore, this protective coating also enables outstanding electrochemical performance under demanding conditions, including high cathode loadings and pouch cell configurations. These findings demonstrate that a rationally designed interfacial layer offers a versatile platform for tackling the multifaceted challenges encountered in aqueous Zn-based energy storage systems.

Author Contributions

Ming Zhao: conceptualization, data curation, validation, Writing – original draft. **Yanjing Wang**: conceptualization, data curation, validation, formal analysis. **Zhihao Li**: validation, formal analysis. **Le Zhou**: formal analysis, visualization. **Mingyu Zhang**: formal analysis. **Hongfei Wang**: conceptualization, writing – original draft, funding acquisition, data curation. **Yong Hu**: conceptualization, funding acquisition, writing – review and editing, supervision, project administration.

Acknowledgements

The authors appreciate the financial support by the National Natural Science Foundation of China (Nos. 22672197 and 22502176) and the Zhejiang Provincial Natural Science Foundation of China (No. LMS26B030007). The calculations were carried out on high performance supercomputer of Zhejiang Normal University.

Conflicts of Interest

The authors declare no conflicts of interest.

Data Availability Statement

The data that support the findings of this study are available in the supplementary material of this article.

References

1. Y. Tan, W. Xu, F. Yang, et al., "Dynamic Polyiodide-Trapping and Proton-Capturing Dual-Network Engineering for High-Areal-Capacity, Long-Cycling and High-Temperature Zn—I 2 Batteries," *Advanced Materials* 38 (2026): e22609, https://doi.org/10.1002/adma.202522609.

2. Q. Zhang, S. Ko, T. Sakata, et al., "Metal Electrode Potential Diverges With Ion Additions," *Nature Chemistry* 18 (2026): 1443–1450, https://doi.org/10.1038/s41557-026-02150-5.

3. S. N. He, R. Zhang, X. Han, et al., "Unraveling 3d Transition Metal (Ni, Co, Mn, Fe, Cr, V) Ions Migration in Layered Oxide Cathodes: A Pathway to Superior Li-Ion and Na-Ion Battery Cathodes," *Advanced Materials* 37 (2025): 2413760, https://doi.org/10.1002/adma.202413760.

4. Y.-L. Liao, X.-L. Wang, H. Yuan, et al., "Ultrafast Li-Rich Transport in Composite Solid-State Electrolytes," *Advanced Materials* 37 (2025): 2419782, https://doi.org/10.1002/adma.202419782.

5. Y. Yuan, Z. Li, R. Deng, et al., "Identifying the Role of Zn Self-Dissolution in the Anode Corrosion Process in Zn-Ion Batteries," *Energy & Environmental Science* 18 (2025): 5610–5621, https://doi.org/10.1039/d5ee00485c.

6. X. Yang, M. Xie, Z. Yan, et al., "High-Iodine-Loading Quasi-Solid-State Zinc–Iodine Batteries Enabled By A Continuous Ion-Transport Network," *Energy & Environmental Science* 18 (2025): 4730–4739, https://doi.org/10.1039/d5ee01170a.

7. F. Yang, L. Zhou, T. Zhang, et al., "A Zincophilic and Negatively-Charged Self-Reconstructed Stratified Interface for Regulating Zn^{2+} Conduction and Nucleation Toward Conformal Dendrite-Free Deposi-

16163028, 2026, 89, Downloaded from https://advanced.onlinelibrary.wiley.com/doi/10.1002/adfm.78682 by Lei Li - Zhejiang Normal University , Wiley Online Library on [10/11/2026]. See the Terms and Conditions (https://onlinelibrary.wiley.com/terms-and-conditions) on Wiley Online Library for rules of use; OA articles are governed by the applicable Creative Commons License

tion," *Angewandte Chemie International Edition* 65 (2026): e23653, https://doi.org/10.1002/anie.202523653.

8. J. Zhong, C. Xia, T. Zhang, et al., "Non-Covalent Molecular Engineering of Hydrogel Electrolytes via π-Anion Confinement and Hydrogen-Bond Reconfiguration for Wide-Temperature and Ultra-Stable Zn-Ion Batteries," *Advanced Functional Materials* 36 (2026): e27894, https://doi.org/10.1002/adfm.202527894.

9. Y. Chen, B. Yin, Y. Zeng, et al., "Ion-Dipole-Interaction-Manipulated Bilateral Interface Chemistry for Deep Rechargeability and High Redox Activity of Zn-Organic Batteries," *Chem* 11 (2025): 102411, https://doi.org/10.1016/j.chempr.2025.102411.

10. Y. Wang, Y. Kong, T. Zhang, C. Chen, H. Wang, and Y. Hu, "Fluorine-Functionalized Chemistry Toward Stable Zn Anode in Aqueous Zn-Ion Batteries," *Advanced Energy Materials* 15 (2025): 2502353, https://doi.org/10.1002/aenm.202502353.

11. X. Xie, L. Sheng, R. Xu, et al., "In Situ Mineralized $Ca_3(PO_4)_2$ Inorganic Coating Modified Polyethylene Separator for High-Performance Lithium-Ion Batteries," *Journal of Electroanalytical Chemistry* 920 (2022): 116570, https://doi.org/10.1016/j.jelechem.2022.116570.

12. Y. Yang, L. Ai, J. He, C. Zhang, D. Chen, and L. Shen, "Stable Lithium Metal Anode Enabled By In Situ Formation of a Li_3N/Li–Bi alloy hybrid layer," *Chemical Communications* 59 (2023): 936–939, https://doi.org/10.1039/d2cc06030b.

13. Z. Xiang, Y. Qiu, X. Guo, K. Qi, Z.-L. Xu, and B. Y. Xia, "Inherited Construction of Porous Zinc Hydroxide Sulfate Layer for Stable Dendrite-Free Zn Anode," *Energy & Environmental Science* 17 (2024): 3409–3418, https://doi.org/10.1039/d4ee00721b.

14. J. Hong, B. Zhu, M. Song, et al., "Fast Ion Transport Interphase Constructed by Hollow Mesoporous $Na_3V_2(PO_4)_3$ for Stable Zinc Anode," *Advanced Functional Materials* 35 (2025): 2424731, https://doi.org/10.1002/adfm.202424731.

15. S. K. Park, S. Kim, R. He, et al., "Synergistic Lithium Alloying and Plating in 3D Cu/CNT/Sn Electrodes for Stable Lithium Metal Batteries," *Small* 21 (2025): 2501292, https://doi.org/10.1002/smll.202501292.

16. T. Wang, Q. Xi, K. Yao, et al., "Surface Patterning of Metal Zinc Electrode With an in-Region Zincophilic Interface for High-Rate and Long-Cycle-Life Zinc Metal Anode," *Nano-Micro Letters* 16 (2024): 112, https://doi.org/10.1007/s40820-024-01377-6.

17. H. Zhu, S. Qiu, M. Sun, et al., "One-Step Constructed F-Doped Porous Carbon-Gradient CuZn Alloy Current Collector for Durable Anode-Less Lithium Metal Batteries," *Advanced Energy Materials* 16 (2026): e70821, https://doi.org/10.1002/aenm.70821.

18. X. Li, Y. Zheng, J. Guo, et al., "Tandem Catalysis Overcomes the Rate-Determining Sulfur Conversion Cascade in Na─S Batteries," *Angewandte Chemie International Edition* 65 (2026): e3876577, https://doi.org/10.1002/anie.3876577.

19. H. R. Lee, G. Lee, S. Lee, et al., "Enhancing Crystallinity of Recycled Carbon Fibers by Synergistic Role of Alkaline Salts and $CaCO_3$ for Lithium-Ion Batteries," *Carbon* 247 (2026): 121042, https://doi.org/10.1016/j.carbon.2025.121042.

20. J. Zhang, G. Li, J. Chen, et al., "Synthesis of Hollow Polyaniline Nanospheres via Surface Tension-Guided Double Emulsion System for Zn Carriers in Aqueous Batteries," *Angewandte Chemie International Edition* 65 (2026): e1886151, https://doi.org/10.1002/anie.1886151.

21. B. Wei, J. Zheng, Abhishek, et al., "Design Principle of Insulating Surface Protective Layers for Metallic Zn Anodes: A Case Study of ZrO_2," *Advanced Energy Materials* 14 (2024): 2401018, https://doi.org/10.1002/aenm.202401018.

22. S. Kim, J. Baek, J. I. Choi, Y.-R. Jo, S. S. Jang, and G.-H. An, "High-Adhesion Zinc Anode Protective Film With Metal-Ion-Doped Conductive Polymer-Coated Carbon Nanotubes for Zinc Ion Batteries," *Nano Energy* 142 (2025): 111203, https://doi.org/10.1016/j.nanoen.2025.111203.

23. Y. Geng, Y. Han, T. Zhang, et al., "Resolving the Zincophilicity-Desolvation Dilemma of Electrolyte Additives via Molecular Engineering for Achieving High-Rate Zinc Anodes With Minimized Polarization," *Advanced Functional Materials* 35 (2025): 2501537, https://doi.org/10.1002/adfm.202501537.

24. S. Zhang, Y. Wu, J. Gao, et al., "High-Entropy Electrolyte for Scalable Zinc–Iodine Flow Batteries," *ACS Energy Letters* 11 (2026): 2247–2256, https://doi.org/10.1021/acsenergylett.5c04158.

25. L. Sun, L. Wang, T. Wang, et al., "Fluorinated MXene-Engineered LiF-Rich Solid Electrolyte Interphase and Hierarchical Confinement Strategy Enabling High Performance Micro-Sized Silicon Anodes," *Nano Research* 19 (2026): 94908024, https://doi.org/10.26599/NR.2025.94908024.

26. S. Yaroshevskyi, A. Adamczyk, N. Brachhold, et al., "Characterization of a Recyclate-Based MgO-Steel Composite as-Sintered Inert Anode Candidate after Exposure to Cryolite Electrolysis," *Advanced Energy Materials* 28 (2026): 202502773, https://doi.org/10.1002/adem.202502773.

27. D. Ma, F. Li, K. Ouyang, et al., "An Electrochemically Driven Hybrid Interphase Enabling Stable Versatile Zinc Metal Electrodes for Aqueous Zinc Batteries," *Nature Communications* 16 (2025): 4817, https://doi.org/10.1038/s41467-025-60190-w.

28. J. B. Dong, G. L. Zhou, W. H. Ding, et al., "Machine Learning-Assisted Benign Transformation of Three Zinc States in Zinc Ion Batteries," *Energy & Environmental Science* 18 (2025): 4872–4882, https://doi.org/10.1039/d5ee00650c.

29. X. Tang, T. Wang, G. Zhou, et al., "Engineering Spatiotemporally-Resolved Hydrogen-Bond Networks for Decoupled H^+ /Zn^{2+} Transport Toward Durable Low-Temperature Aqueous Zinc-Ion Batteries," *Advanced Energy Materials* 16 (2026): 71050, https://doi.org/10.1002/aenm.71050.

30. Z. W. Hu, L. Y. Liu, X. Wang, et al., "Situ Integration of Rapid Ion-Diffusion Interlayers on Cu Current Collectors Toward Ultrafast Anode-Free Sodium Metal Batteries," *ACS Nano* 19 (2025): 23193–23208, https://doi.org/10.1021/acsnano.5c05043.

31. Z. Liu, S. Chen, Z. Shi, et al., "Multivalent Dipole Interactions-Driven Supramolecular Polymer Layer Enables Highly Stable Zn Anode Under Harsh Conditions," *Advanced Energy Materials* 15 (2025): 2502010, https://doi.org/10.1002/aenm.202502010.

32. R. C. Guzman, K. L. Montero, and M. Mäntysalo, "Fully Printed Multilayer Flexible Structure for 3D Assembly on Irregular Substrates for Hybrid Electronics," *Advanced Electronic Materials* 12 (2026): e70456, https://doi.org/10.1002/aelm.70456.

33. X. Liu, L. Zhang, X. Chen, et al., "Precision Interface Architecture of Zinc Anodes for Highly Reversible Zn-Metal Batteries," *Chemical Engineering Journal* 529 (2026): 172666, https://doi.org/10.1016/j.cej.2026.172666.

34. Y. Li, T. Han, M. Zhao, et al., "Modulating Interfacial Shear of Nanoconfined Hydration Layer via Surface Charging," *Nano Energy* 148 (2026): 111692, https://doi.org/10.1016/j.nanoen.2025.111692.

35. J. Bu, P. Liu, G. Ou, et al., "Interfacial Adsorption Layers Based on Amino Acid Analogues to Enable Dual Stabilization Toward Long-Life Aqueous Zinc Iodine Batteries," *Advanced Materials* 37 (2025): 2420221, https://doi.org/10.1002/adma.202420221.

36. C. Li, Y. Cai, P. Hu, et al., "Organic Solar Cells With 21% Efficiency Enabled by a Hybrid Interfacial Layer With Dual-Component Synergy," *Nature Materials* 24 (2025): 1626–1634, https://doi.org/10.1038/s41563-025-02305-8.

37. G. J. Li, Z. H. Zhao, S. L. Zhang, et al., "A Biocompatible Electrolyte Enables Highly Reversible Zn Anode for Zinc Ion Battery," *Nature Communications* 14 (2023): 6526, https://doi.org/10.1038/s41467-023-42333-z.

38. H. Xue, Y. Wu, Z. Wang, et al., "Unraveling the New Role of Metal–Organic Frameworks in Designing Silicon Hollow Nanocages for High-Energy Lithium-Ion Batteries," *ACS Applied Materials & Interfaces* 13 (2021): 40471–40480, https://doi.org/10.1021/acsami.1c07495.

16163028, 2026, 89, Downloaded from https://advanced.onlinelibrary.wiley.com/doi/10.1002/adfm.78682 by Lei Li - Zhejiang Normal University , Wiley Online Library on [10/11/2026]. See the Terms and Conditions (https://onlinelibrary.wiley.com/terms-and-conditions) on Wiley Online Library for rules of use; OA articles are governed by the applicable Creative Commons License

39. Y. Zhou, Y. Pan, Y. Yang, et al., "Electrically Insulating Rigid Multi-Channel Electrolyte Container for Customizable Electron Transfer in Zn-Halogen Batteries," *Nano-Micro Letters* 18 (2026): 168, https://doi.org/10.1007/s40820-025-02007-5.

40. C. Chen, M. Zhao, T. Zhang, K. Xie, H. Wang, and Y. Hu, "Lewis Acid-Base Mediated MOF-Polymer Hydrogel Electrolyte for Oriented Ion Conduction and Textured Zn (002) Deposition," *Composites Part B: Engineering* 309 (2026): 113053, https://doi.org/10.1016/j.compositesb.2025.113053.

41. L. Wang, B. Zhang, W. Zhou, et al., "Tandem Chemistry With Janus Mesopores Accelerator for Efficient Aqueous Batteries," *Journal of the American Chemical Society* 146 (2024): 6199–6208, https://doi.org/10.1021/jacs.3c14019.

42. P. Li, Z. Hu, Z. Wen, et al., "Regulating Dynamic Solid Electrolyte Interfacial Evolution via α-H Methyl Substitution Carboxylate Ester Electrolytes Toward 20 Ah Wide-Temperature (−60°C–70°C) Li-Ion Pouch Cells," *Angewandte Chemie International Edition* 65 (2026): e21079, https://doi.org/10.1002/anie.202521079.

43. Z. Xu, Z. Liu, Z. Shi, R. Wang, S. Chen, and T. Liu, "Molecularly Engineered Self-Healing Polymer Interphase With Synergistic Dipoles for Ultra-Stable Zinc Metal Anodes," *Advanced Functional Materials* 36 (2026): e77450, https://doi.org/10.1002/adfm.77450.

44. Y. Wang, L. Zhou, T. Zhang, W. Gao, H. Wang, and Y. Hu, "An Oligomeric Additive Bridges Inner and Outer Helmholtz Planes to Enable Reversible Zn Anodes via Spatial and Functional Decoupling," *Angewandte Chemie International Edition* 65 (2026): e2336331, https://doi.org/10.1002/anie.2336331.

45. A. Tuladhar, S. Dewan, S. Pezzotti, et al., "Ions Tune Interfacial Water Structure and Modulate Hydrophobic Interactions at Silica Surfaces," *Journal of the American Chemical Society* 142 (2020): 6991–7000, https://doi.org/10.1021/jacs.9b13273.

46. J. Xu, H. Gu, Y. Wu, et al., "Sub-Nano Confinement Engineering Toward Anion-Reinforced Solvation Structure to Achieve Highly Reversible Anode-Free Lithium Metal Batteries," *Advanced Energy Materials* 15 (2025): 2405196, https://doi.org/10.1002/aenm.202405196.

47. M. Xu, X. He, S. Xue, et al., "Unveiling Ion Pairing Reorganization Mechanism of Oxygen Vacancy-Rich Amorphous Molybdenum Oxide-Based Solid-Electrolyte Interphase for Fast Zn^{2+} Desolvation," *Advanced Energy Materials* 16 (2026): 03167, https://doi.org/10.1002/aenm.202503167.

48. H. Kang, J. B. Park, M. Jang, M. S. Kim, S. Yu, and D.-W. Kim, "Synergistically Accelerating Zn^{2+} Transport and Desolvation Through Cation-Deficient Ion Channels in High-Performance Zn Metal Batteries," *Carbon Energy* 8 (2026): 70303, https://doi.org/10.1002/cey2.70303.

49. Y. Song, H. Liang, J. Guo, et al., "Harmonized Multifaceted Zinc Deposition Enabled by Amine-Functionalized Carbon Quantum Dots for Dendrite-Free Zinc Anodes Under Ultrahigh Current Densities," *Carbon Energy* 8 (2026): 70284, https://doi.org/10.1002/cey2.70284.

50. K. Ye, T. Qiu, J. Wan, et al., "Synergetic Effect of Multicomponent Phosphate and Rich Grain-Boundary in Solid/Electrolyte Interphase Boosts Rapid Ion Transport Toward Fast Aqueous Zinc Metal Batteries," *Advanced Energy Materials* 15 (2025): 2502125, https://doi.org/10.1002/aenm.202502125.

51. D. Xu, Z. Wang, C. Liu, et al., "Water Catchers Within Sub-Nano Channels Promote Step-by-Step Zinc-Ion Dehydration Enable Highly Efficient Aqueous Zinc-Metal Batteries," *Advanced Materials* 36 (2024): 2403765, https://doi.org/10.1002/adma.202403765.

52. G. Li, S. Zhang, J. A. Yuwono, et al., "Hydrophobic Liquid Electrolyte Interphases for Efficient Aqueous Zinc Batteries," *Nature Nanotechnology* 21 (2026): 967–975, https://doi.org/10.1038/s41565-026-02187-0.

53. Y. Shao, J. Chen, T. Zhang, et al., "Concentration-Gradient Engineered Dual-Mode Zn^{2+} Transport for Highly Reversible Dendrite-Free Zn Anodes," *Chemical Engineering Journal* 524 (2025): 169181, https://doi.org/10.1016/j.cej.2025.169181.

54. C. Lin, L. Zeng, M. Liu, et al., "Dynamic Regulation for the Well-Distribution of Electrons and Zn^{2+} Ions Achieving Uniform Zn Redox in Ah-Scale Pouch Cells," *Advanced Materials* 37 (2025): e11484, https://doi.org/10.1002/adma.202511484.

55. Y. Dai, W. Du, H. Dong, et al., "Mitigating Ion Flux Vortex Enables Reversible Zinc Electrodeposition," *Nature Communications* 16 (2025): 7312, https://doi.org/10.1038/s41467-025-62470-x.

56. K. Gao, Z. Li, G. I. N. Waterhouse, and Z. Wang, "Tunnel-Framework Interphase Driving Rapid Zn^{2+} Diffusion for Long-Life Zn Metal Anodes," *Advanced Energy Materials* 16 (2026): e71196, https://doi.org/10.1002/aenm.71196.

57. L. Mao, G. Li, C. Wang, et al., "Reversing the Hofmeister Response in Hydrogels via Anion Affinity Chemistry," *Journal of the American Chemical Society* 148 (2026): 25037–25049, https://doi.org/10.1021/jacs.6c05631.

58. X. Fu, Y. Pan, Z. Chen, et al., "An Amino Acid-Based Functional Additive Enables Fast Polyiodide Conversion Kinetics for Durable Zn–I_2 Batteries," *Energy & Environmental Science* 19 (2026): 1170–1179, https://doi.org/10.1039/d5ee06668a.

59. Y. Wang, K. Zhong, J. Zhang, et al., "Concomitant Zinc Dendrite Mitigation and Iodide Shuttle Confinement: A Bifunctional Zwitterionic Hydrogel Electrolyte Unlocking Ultralong-Cycling Aqueous Zinc-Iodine Batteries," *Advanced Functional Materials* 36 (2026): e26937, https://doi.org/10.1002/adfm.202526937.

60. D. Yin, B. Li, L. Zhao, et al., "Polymeric Iodine Transport Layer Enabled High Areal Capacity Dual Plating Zinc-Iodine Battery," *Angewandte Chemie International Edition* 64 (2025): e202418069, https://doi.org/10.1002/anie.202418069.

61. Z. Bai, G. Wang, H. Liu, et al., "Advancements in Aqueous Zinc–Iodine Batteries: A Review," *Chemical Science* 15 (2024): 3071–3092, https://doi.org/10.1039/d3sc06150g.

62. S. Ali, D. Hussain, B. Hussain, M. A. Parvez, and M. Rahaman, "Interface-Centered Design of Practical Aqueous Zinc Batteries: Solvation Regulation, Interphase Engineering, and Full-Cell Stability," *Coordination Chemistry Reviews* 568 (2026): 218435, https://doi.org/10.1016/j.ccr.2026.218435.

Supporting Information

Additional supporting information can be found online in the Supporting Information section.

Supporting File: adfm78682-sup-0001-SuppMat.doc.

16163028, 2026, 89, Downloaded from https://advanced.onlinelibrary.wiley.com/doi/10.1002/adfm.78682 by Lei Li - Zhejiang Normal University , Wiley Online Library on [10/11/2026]. See the Terms and Conditions (https://onlinelibrary.wiley.com/terms-and-conditions) on Wiley Online Library for rules of use; OA articles are governed by the applicable Creative Commons License